JMEPEG (2024) 33:3801–3810
https://doi.org/10.1007/s11665-023-08904-3

©ASM International
1059-9495/$19.00

ORIGINAL RESEARCH ARTICLE

Investigation of Residual Stresses Induced by Milling of Compacted Graphite Iron by x-ray Diffraction Technique

Mehmet Emre Kara, Ali Taner Kuzu, and Mustafa Bakkal

Submitted: 8 June 2023 / Revised: 16 September 2023 / Accepted: 23 October 2023 / Published online: 6 November 2023

This study investigates the relationship between residual stresses, cutting parameters, and machining performance in the milling process of compacted graphite iron (CGI). X-ray diffraction (XRD) analysis is employed to measure residual stresses on the cast and milled surfaces, while cutting force modeling is utilized to calculate the tangential force, power, and active work. The results demonstrate that tensile residual stresses are predominant on the milled surfaces, attributed to the both mechanical and thermal loads generated during milling. By analyzing various cutting conditions, it is observed that lower feeds contribute to reduced plastic deformation, resulting in lower residual stress levels. Additionally, higher cutting speeds lead to higher temperatures, but due to the shorter machining time, heat accumulation is limited, resulting in higher residual stresses, especially at low feeds. At high feeds, residual stresses decreased as the cutting speed increased. The interplay between cutting parameters and residual stresses highlights the need for optimizing cutting conditions to enhance fatigue strength in CGI components. These findings provide valuable insights for process optimization and quality control in the milling of CGI materials.

Keywords compacted graphite iron, cutting parameters, milling, residual stress, x-ray diffraction

1. Introduction

Residual stresses in the surface and subsurface regions of a machined component play a crucial role in determining its performance during service. These stresses are considered the most significant factors in assessing surface integrity. Depending on their nature, residual stresses can either enhance or impair the lifespan of manufactured parts. Research (Ref 1) has shown that compressive stresses offer advantages such as improved fatigue life, resistance to creep, and enhanced resistance to stress corrosion cracking. Conversely, tensile residual stresses tend to have detrimental effects on these properties. Therefore, understanding the characteristics of residual stresses in the machined surface and subsurface regions is highly valuable for product design and manufacturing processes.

In recent times, compacted graphite iron (CGI) has gained significant attention, particularly from engine manufacturers, due to its potential for long service life as an integral component of internal combustion engines. CGI possesses physical and mechanical properties that lie between gray and spheroidal cast irons (Ref 2). These properties offer a favorable balance, making CGI more advantageous compared to other cast iron materials. For instance, the higher strength of CGI surpasses that of gray cast irons, while its superior thermal conductivity, in comparison with spheroidal cast irons, is particularly desirable for engine components exposed to high pressures and temperatures, such as engine blocks and cylinder heads. The production of these intricate geometry parts involves casting and machining processes. To comprehend the mechanical performance of CGI following these manufacturing steps, it is essential to measure residual stresses. Understanding the distribution and types of residual stresses enables the anticipation of fatigue and tensile properties in CGI specimens (Ref 3-5).

In recent years, numerous studies have focused on investigating residual stresses generated by different metal removal methods. These investigations have primarily concentrated on high-strength materials and employed various processes such as turning, drilling, grinding, and electrical discharge machining (EDM) (Ref 6-12). The distribution of residual stresses on the surface region of a machined workpiece has been observed to be influenced by factors such as cutting speed, feed, depth of cut, tool geometry, and the use of lubricants specific to the workpiece material. The magnitude of residual stress near the

This invited article is part of a special topical issue of the *Journal of Materials Engineering and Performance* on Residual Stress Analysis: Measurement, Effects, and Control. The issue was organized by Rajan Bhambroo, Tenneco, Inc.; Lesley Frame, University of Connecticut; Andrew Payzant, Oak Ridge National Laboratory; and James Pineault, Proto Manufacturing on behalf of the ASM Residual Stress Technical Committee.

Mehmet Emre Kara, Mechanical Engineering Department, Istanbul Technical University, 34437 Istanbul, Turkey; and Rail Transport Technologies Institute, TUBITAK, 41470 Kocaeli, Turkey; **Ali Taner Kuzu**, Mechanical Engineering Department, Isik University, 34980 Istanbul, Turkey; and **Mustafa Bakkal**, Mechanical Engineering Department, Istanbul Technical University, 34437 Istanbul, Turkey. Contact e-mail: karame@itu.edu.tr.

surface is significant and gradually decreases with increasing depth beneath the machined surface. Under conditions of high depths of cut with worn tools and in the absence of a lubricant, residual stresses tend to be tensile. However, they can become compressive when machining at shallow depths of cut with sharp tools and in the presence of a lubricant (Ref 13).

Residual stresses can be generated due to the inhomogeneous plastic deformation resulting from mechanical and thermal phenomena associated with chip formation and the contact between the tool nose region and the freshly machined workpiece surface (Ref 14). However, there is currently no precise understanding of how changes in cutting conditions during milling of compacted graphite iron affect the characteristics of the residual stress distribution in the surface region.

The objective of this study is to examine the residual stresses in compacted graphite cast iron following the casting and milling processes, as well as to analyze the impact of various cutting parameters on the residual stresses on the surface of the component. To achieve this goal, the non-destructive x-ray diffraction method was selected. This method has been widely used for measuring residual stresses in crystalline materials and is based on the principle of measuring changes in lattice spacing caused by residual stresses through the diffraction of an x-ray beam with a single wavelength (λ) in polycrystalline materials. Details of this method are given in Section 2.2.

2. Materials and Methods

The material used for the workpieces in this study was GJV-400 (EN 16079), cast at the Doktas iron casting plant. The chemical components and properties of the material are provided in Table 1 and 2, respectively. Each specimen was individually cast, ensuring uniform cooling conditions and consistent microstructure and mechanical properties. Prior to the experiments, the workpieces were subjected to rough machining on the top, bottom, and sides to obtain rectangular blocks measuring 100 mm (length) × 30 mm (width) × 30 mm (height). This machining step was performed to remove the hardened cast skin and achieve optimal clamping conditions.

2.1 Milling Experiments

The cutting tests were conducted using a vertical CNC machining center, specifically the Spinner VC-650 model, with a maximum spindle speed of 8000 rpm. The machining center, with a power rating of 16.5 kW, features an SK40 taper where a milling cutter was mounted. The selected face milling cutter for this study had a diameter (D) of 50 mm, with the specification R365-050Q22-S15H. The cutter was equipped with 5 evenly distributed CVD (TiCN + Al_2O_3)-coated cemented carbide inserts, each having the specification R365-1505ZNE-KM K20D.

Due to the complex geometry of many industrial parts, the tool enters the part at different entry and exit angles during machining. In addition, the difference in cooling rates after casting in CGI results in strength differences between thick and thin sections within the part. This causes load variations during machining. Considering such different scenarios, it was decided to perform center-face milling, which covers more scenarios, instead of up or down milling. A schematic representation of the center-face milling process is shown in Fig. 1. Here, f is the feed (mm/rev) and is calculated according to Eq 1, where f_t is the feed per tooth (mm/tooth) and z is the number of teeth of the tool, in our experiments the tool has 5 teeth (inserts) as mentioned before. n is the spindle speed and is used to calculate the cutting speed according to Eq 2.

$$f = f_t \cdot z \quad \text{(Eq 1)}$$

$$V_c = \pi \cdot D \cdot n \quad \text{(Eq 2)}$$

The axial cutting depth was maintained at a constant value of 1 mm throughout the study. For the experiments, three different cutting speeds (V_c) and two different feeds per tooth (f_t) were selected as parameters.

The specific milling parameters used in the experiments can be found in Table 3.

While cutting fluid is commonly employed during the milling of cast iron, primarily to bind graphite particles and clear away chips from the cutting area rather than extending tool life, it is advised to refrain from using cutting fluid when milling compacted graphite iron (CGI). Instead, alternative methods such as vacuum equipment should be utilized to manage the generated dust (Ref 15). Consequently, all cutting tests in this study were conducted under dry conditions. The experimental setup for milling CGI workpieces is illustrated in Fig. 2. Each specimen underwent a single pass during the milling process.

Table 1 Chemical compositions of the GJV-400 material

Element	C	Si	Mn	S	P	Cr	Ni	Cu	Mg	Sn	Ti
Content, %	3.79	2.26	0.27	0.022	0.012	0.06	0.014	0.38	0.014	0.04	0.022

Table 2 Physical and mechanical properties of the GJV-400 material

Ultimate tensile strength, MPa	Yield stress, MPa	Elongation, %	Young's modulus, GPa	Hardness, HBW	Thermal conductivity, W/(m K)	Thermal expansion, μm/(m K)	Specific heat capacity, J/(kg K)
400	310	2	145	210	39	11	475

2.2 Principles of XRD Method and XRD Measurements

During elastic deformation of a polycrystalline material, where strain is evenly distributed over a considerable distance, the lattice spacing within individual crystals undergoes a change from its stress-free value to a new value determined by the magnitude of the applied stress. This phenomenon is governed by Bragg's law (Ref 16), which states that the new spacing (d_{hkl}) remains consistent across crystals for specific sets of crystal planes (hkl). However, as a result of the uniform strains, the lattice spacing experiences alterations, leading to a corresponding shift in the angle (2θ) between the incident and diffracted beams (Ref 17).

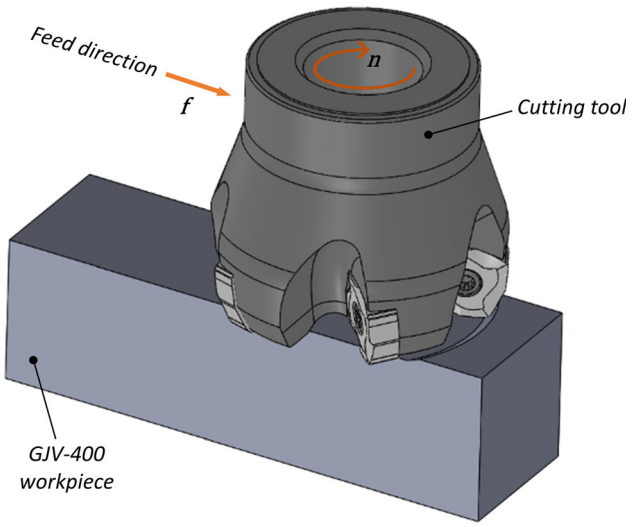

Fig. 1 Schematic representation of the center-face milling

Table 3 Milling parameter set

Experiment #	Cutting speed, m/min	Feed per tooth, mm/tooth
1	150	0.15
2	150	0.3
3	300	0.15
4	300	0.3
5	450	0.3

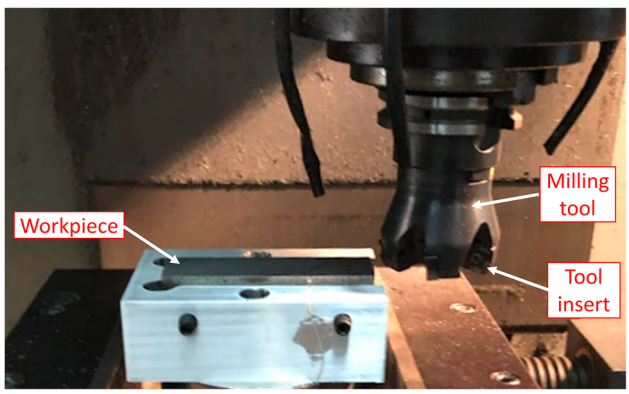

Fig. 2 Experimental setup for the CGI milling process

Understanding the behavior of lattice spacing changes during elastic deformation is crucial for comprehending the material's response to external forces. It provides insights into the internal structural modifications occurring within the material's crystalline structure. These changes in lattice spacing, induced by the applied stress, can influence various material properties, such as mechanical behavior, electrical conductivity, and thermal expansion. Therefore, the study of lattice spacing alterations plays a vital role in understanding the mechanical and physical properties of polycrystalline materials.

Figure 3 shows the interaction between incident and diffracted beams on a crystal lattice, providing insights into lattice spacing changes and diffraction angle shifts. This information helps understand internal stress distribution and lattice distortion in polycrystalline materials. Plastic deformation causes distortion in lattice planes and variations in lattice spacing. The x-ray diffraction (XRD) technique focuses on beams with uniform strain-induced shifts, allowing calculation of strain along specific crystallographic planes. Figure 4 illustrates the distribution and orientation of principal stresses within a stressed polycrystalline material.

To measure the stress (σ_ϕ) along an arbitrary direction on the surface, which forms an angle (ϕ) with the direction of the principal stress (σ_{11}), the x-ray diffraction (XRD) method can be employed, allowing measurements to be taken at any chosen angle (as shown in Fig. 4).

According to Noyan and Cohen (Ref 19), Eq 3-11 represent the fundamental equations of x-ray strain determination and stress analysis.

The strain ε_3 can be expressed as a function of the principal stresses, considering the Poisson's ratio:

$$\varepsilon_3 = \varepsilon_{\phi,\,\psi=0} = -\frac{v}{E}(\sigma_{11}+\sigma_{22}) \qquad \text{(Eq 3)}$$

The value of ε_3 can be found using Eq 4:

$$\varepsilon_3 = \frac{d_n - d_0}{d_0} \qquad \text{(Eq 4)}$$

The unstrained interplanar spacing is represented as d_0, while d_n (also denoted as $d_{\phi,\psi=0}$) corresponds to the spacing between (hkl) planes parallel to the surface. This value, d_n, can be determined experimentally by measuring the peak position (2θ) and solving for d_n according to Bragg's law given in Eq 5.

$$n\lambda = 2d_{hkl}\sin\theta \qquad \text{(Eq 5)}$$

When Eq 3 and 4 are equated:

$$\varepsilon_3 = \frac{d_n - d_0}{d_0} = -\frac{v}{E}(\sigma_{11}+\sigma_{22}) \qquad \text{(Eq 6)}$$

In order to obtain the value of σ_ϕ, it is essential to acquire two strain measurements: ε_3 along the surface normal and $\varepsilon_{\phi\psi}$ at an angle ψ with the surface normal, as depicted in Fig. 4. By employing the principles of Hooke's elasticity theory, the strain in the desired direction can be determined.

$$\varepsilon_{\phi\psi} = \frac{1}{E}\left[\sigma_\phi(1+v)\sin^2\psi - v(\sigma_{11}+\sigma_{22})\right] \qquad \text{(Eq 7)}$$

Equation 7 is a form of the traditional x-ray residual stress equation and has been in use for over 90 years (Ref 20). It provides the lattice strain along a line inclined to the angle ψ with respect to the Phi angle ϕ and predicts a linear variation of d versus $\sin^2\psi$. The determination of stress in the ϕ direction

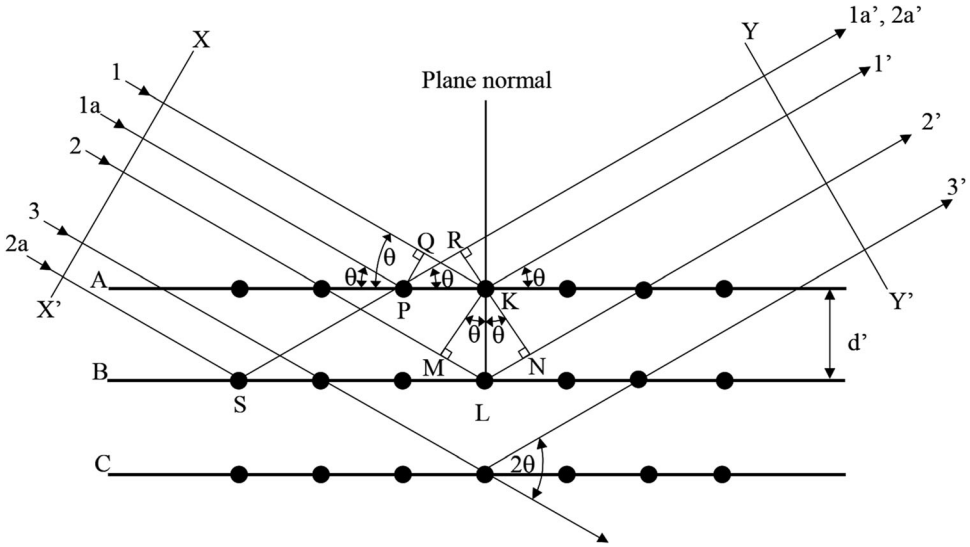

Fig. 3 Diffraction of x-rays by a crystal lattice (Ref 18). Source: M.E. Fitzpatrick, A.T. Fry, P. Holdway, F.A. Kandil, J. Shackleton, and L. Suominen, Determination of Residual Stresses by x-ray Diffraction —Issue 2, NPL, 2005

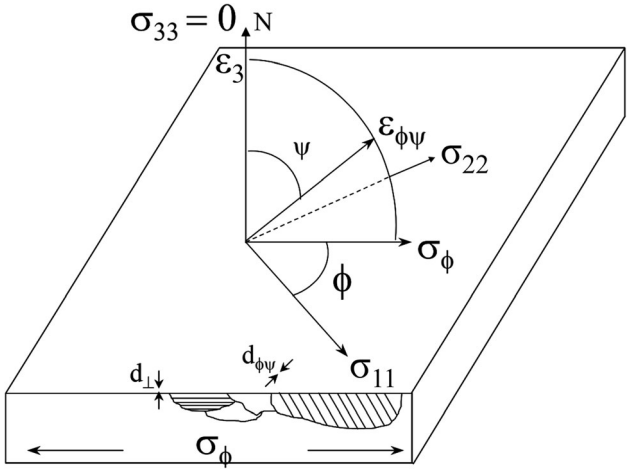

Fig. 4 Stress in the biaxial system and definition of angles ϕ and ψ (Ref 18). Source: M.E. Fitzpatrick, A.T. Fry, P. Holdway, F.A. Kandil, J. Shackleton, and L. Suominen, Determination of Residual Stresses by x-ray Diffraction—Issue 2, NPL, 2005

can be directly obtained by analyzing the slope of a least-squares line fitted to experimental data collected at various ψ angles, given that the elastic constants E and ν, along with the unstressed plane spacing denoted as d_0, are available. This methodology is referred to as the "$\sin^2\psi$" technique (Ref 21), named so due to its utilization of multiple ψ-tilt measurements.

By subtracting Eq 4 from Eq 7, we find;

$$\varepsilon_{\phi\psi} - \varepsilon_3 = \frac{\sigma_\phi}{E}(1+\nu)\sin^2\psi \qquad \text{(Eq 8)}$$

The x-ray diffraction technique is based on a fundamental principle described by the equation mentioned above. This equation highlights that the variation in strains caused by different stress components is determined solely by the orientation of the respective planes. By rearranging Eq 8 in terms of plane spacing, we can establish the following relationship:

$$\frac{d_{\phi\psi} - d_0}{d_0} - \frac{d_n - d_0}{d_0} = \frac{d_{\phi\psi} - d_n}{d_0} = \frac{\sigma_\phi}{E}(1+\nu)\sin^2\psi \qquad \text{(Eq 9)}$$

Equation 10, a rearrangement of Eq 9, allows us to calculate the stresses in any arbitrary directions employing the inter-planar spacing measurements that made in a plane normal to the specimen surface and in the direction of the stress to be measured.

$$\sigma_\phi = \frac{E}{(1+\nu)\sin^2\psi}\left(\frac{d_{\phi\psi} - d_n}{d_0}\right) \qquad \text{(Eq 10)}$$

The 2θ–$\sin^2\psi$ graph is a graphical representation that illustrates the relationship between the diffraction angle (2θ) and the square of the sine of the tilt angle ($\sin^2\psi$) in x-ray diffraction measurements. It is commonly used in XRD analysis to investigate the behavior of diffraction peaks and to determine various properties of the material being studied, such as lattice spacing, crystal orientation, and residual stress. By analyzing the 2θ–$\sin^2\psi$ graph, valuable information about the residual stress distribution and its effects on the material can be obtained.

In this study, the $\sin^2\psi$ method was employed to assess the residual stresses. This method involved measuring the lattice spacing ($d_{\phi\psi}$) at various positive and negative ψ-tilt angles. Through the use of the least square method, a linear regression model of the form $y = mx + d_n$ was fitted to the measured inter-planar spacing values ($d_{\phi\psi}$ or 2θ peak position) plotted against $\sin^2\psi$. By calculating the slope of the fitted line (m) and incorporating the elastic properties of the material, such as the Poisson's ratio (ν) and Young's modulus (E), the stress can be determined. It is assumed that the stress is zero at $d = d_n$, where d represents the y-intercept when $\sin^2\psi = 0$. By substituting the slope and y-intercept values into Eq 10, the residual stress values can be calculated for the desired direction (ϕ).

$$\sigma_\phi = \frac{E}{(1+\nu)}\frac{m}{d_{\phi,\psi=0}} \qquad \text{(Eq 11)}$$

For the x-ray residual stress measurements, a Rigaku SmartLab diffractometer with a Cu Kα source

(λ = 1.541862 Å) was utilized. To eliminate diffractions other than Cu Kα, the Cu Kβ filter was used. The device was operated at a voltage of 45 kV and a current of 200 mA for all measurements. The experimental setup can be seen in Fig. 5. To obtain the slope and intercept for the 2θ versus $\sin^2\psi$ graph, 12 different Psi tilt angles ranging from − 5° to + 45° were utilized. Parallel beam (PB) optics were used in the goniometer and the PSA mirror angle was 0.5 degrees. When the diffraction angle is evaluated according to the measurement direction, the side-inclination method was used in our study. In this method, the diffraction angle is measured by setting the detector scanning plane perpendicular to the psi plane. The Young's modulus and Poisson's ratio used for GJV-400 were taken as 145 GPa and 0.26, respectively, according to ISO 16112–CGI classification standard (Ref 22).

Some features of the XRD device used are given below (Ref 23):

- High-flux x-ray source: PhotonMax
- HyPix-3000 high energy resolution HPAD (hybrid pixel array detector)
- 9 kW rotating anode x-ray source with semiconductor detector supporting 0D, 1D or 2D x-ray diffraction measurement modes.
- High-resolution θ/θ closed loop goniometer drive system with in-plane diffraction arm.
- Fully computer-controlled alignment system that can be operated with different measurement modes.

Prior to commencing the analysis of residual stress, it is advantageous to determine the peak angle values of the material. This can be achieved by examining the "2-theta – intensity" graph obtained for the material. By substituting the angle into Bragg's law formula, the spacing distance between the lattice planes of the material in its stress-free state can be calculated. Figure 6 illustrates the "2-theta – intensity" graph, which represents the XRD pattern of GJV-400.

In order to improve the resolution of the peaks, the scanning speed was set to 0.2 deg/min, the step width to 0.06°, and the incident slit to 1 mm to match the width of the analysis zone. Due to the high texture in the material, it was observed that the peaks disappeared in the residual stress measurement according to different ψ angles at high peak angles such as 117.5°, and 99°. Generally, the intensity is expected to be more than 1000 counts in residual stress measurements. As a result of the experiments, it was observed that the most reliable results were realized at 82.5° and the intensity did not fall below 1000 counts at all ψ values.

The important parameters considered during XRD measurements are listed in Table 4.

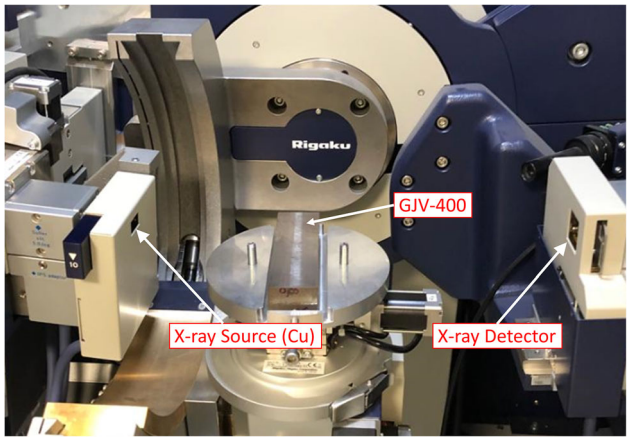

Fig. 5 Experimental setup of x-ray diffraction for residual stress characterization

3. Results and Discussions

The XRD residual stress data were analyzed using different tilt (psi) angles in the (211) diffraction plane, and the detection was performed at approximately a diffraction angle of 82.5°. Figure 7 presents the 2θ–$\sin^2\psi$ graphs for both the cast specimen and the milled workpieces, corresponding to the parameters specified in Table 3. These graphs provide valuable insights into the types of residual stresses present on the surfaces of the parts, their magnitudes, and the corresponding residual stress equations.

When Fig. 7(a) is examined, compressive residual stress was detected on the surface of the cast specimen. When Fig. 7(b) to (f) are examined, tensile residual stresses due to the machining effect were observed on the surface of the GJV-400 specimen milled with different cutting parameters. The residual stress values obtained from the casting surface and milled surfaces are listed in Table 5.

The effects of cutting parameters on residual stresses are given in Fig. 8. While the residual stress increased with increasing feed, there was no linear correlation between cutting speed and residual stress. In the literature also, some researchers found that the residual stresses increased with cutting speed (Ref 24-26) while others found the opposite outcome (Ref 27-31). In a related study, Sun and Guo (Ref 32) found that increasing the feed leads to an increase in the magnitude of residual tensile stresses on the workpiece surface. Wu et al. (Ref 33) observed that the effect of feed exceeds the effect of milling speed, while Prakash et al. (Ref 34) highlighted that feed has the most significant effect on residual stress generation.

The tangential force, power, and active work values varying according to the cutting parameters in the milling operation are also given in Table 5 and are considered to be useful in interpreting the residual stress results. These values were calculated according to the cutting force model proposed by Kara et al. (Ref 35) for milling GJV-400 material. The active work is expressed as the product of power and machining time. In the same study, the relationship between the active work and the temperature distribution in the workpiece after milling was mentioned. They showed that the higher the calculated active work, the higher the temperatures generated on the workpiece and vice versa.

Plastic deformations and thermal loads on the part during the milling process cause residual stresses. These mechanical and thermal loads are affected by the workpiece material, cutting parameters (cutting speed, feed, depth of cut), and tool geometry (rake and oblique angle). When the residual stress data of CGI material during milling are analyzed, it is seen that the residual stresses are predominantly in the tensile region. In general, mechanical loads cause compressive residual stresses in the part, as found in the part after shot peening or sand-blasting operations (Ref 36). However, mechanical loads

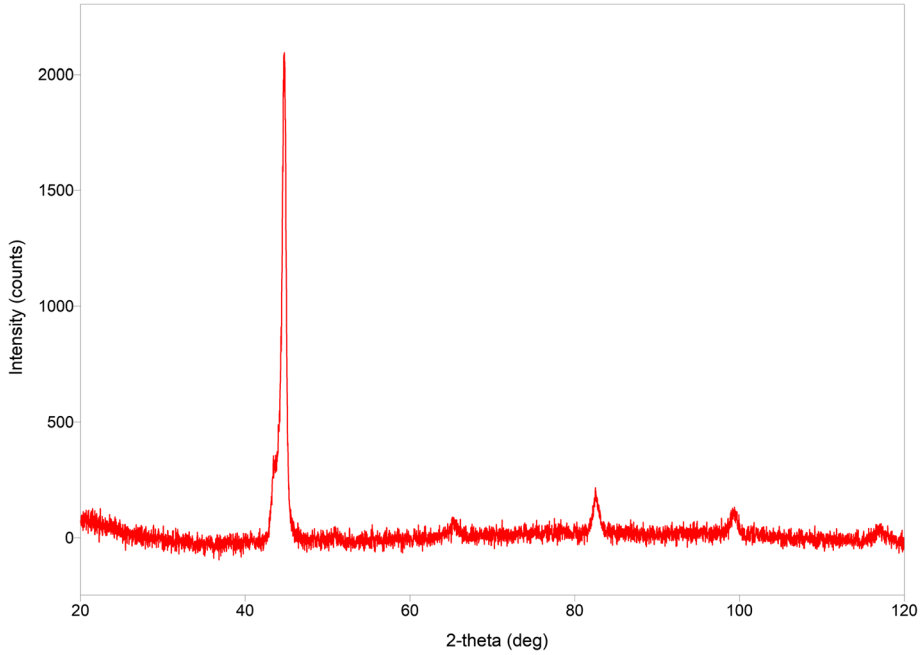

Fig. 6 Peak values obtained from the GJV-400 by XRD measurements

Table 4 XRD setup parameters

Parameter	Type/value
Mode	$\sin^2 \psi$
ψ positions	Between − 5° and + 45°
Radiation	Cu Kα
Wavelength	1.541862 Å
Voltage and current	45 kV, 200 mA
Peak, h,k,l	82.5° (211)

caused by machining tend to produce tensile residual stress on the part surface (Ref 37). This is mostly due to the ploughing force between the workpiece and the tool (Ref 37). Residual stress caused by the thermal effect is always tensile as far as coolant is not used (Ref 37).

The experimental results presented in Table 5 provide valuable information on the relationship between cutting parameters and the resulting residual stresses, tangential force, power, and active work.

Analyzing the data, it is evident that all the residual stress values observed during the milling operations were positive, indicating the presence of tensile residual stresses on the milled surfaces. This finding indicates that the milling has a reducing effect on the fatigue strength of CGI material.

Examining the specific experiments, Experiment 1, was conducted with a cutting speed of 150 m/min and a feed of 0.15 mm/tooth, resulting in a residual stress of 111 ± 12 MPa. This experiment exhibited the lowest residual stress among all the milling conditions tested. This observation suggests a lower feed contributes to reduced plastic deformation. Low cutting speed, on the other hand, leads to heat accumulation and elevated surface temperatures, resulting in delayed cooling and higher residual stress. However, when the effects of mechanical and thermal loads are considered separately, it is seen that mechanical loads are more effective on the residual stress.

In contrast, Experiment 2, performed with the same cutting speed of 150 m/min but a higher feed of 0.3 mm/tooth, showed significantly higher residual stress of 224 ± 16 MPa. While it is desirable that the high feed prevents heat accumulation on the part, the significant plastic deformation caused an increase in residual stresses on the part surface.

Moving on to Experiments 3 and 4, conducted at a higher cutting speed of 300 m/min, but with feeds of 0.15 mm/tooth and 0.3 mm/tooth, respectively, different effects on residual stresses were observed. Experiment 3 resulted in a residual stress of 196 ± 22 MPa, while Experiment 4 yielded a considerably higher value of 283 ± 21 MPa. Increasing the cutting speed from 150 to 300 m/min caused an increase in the temperature during milling, resulting in higher residual stresses compared to Experiments 1 and 2.

When the workpiece surface milled with 450 m/min cutting speed and 0.3 mm/tooth feed was examined, it was observed that although the high cutting speed caused an increase in temperatures during milling, the shorter machining time limited heat accumulation, and this resulted in lower residual stresses. While the heat generated by the cutting speed was more dominant in Experiments 3 and 4, the fact that the cutting process was completed in a much shorter time in Experiment 5 prevented heat accumulation in the part, and a decrease in residual stress was observed compared to Experiment 4.

The tangential force (N), power (W), and active work (J) values listed in Table 5 indicate the mechanical energy involved in the milling process for each experiment. Considering that the tangential force represents the mechanical loads, and the power and active work together represent thermal loads, the effect of these two loads jointly on the residual stresses can be examined in Fig. 9. Here, the residual stresses increase with thermal effects, but it is seen that mechanical loads have a more dominant effect than thermal loads. It was observed that power at low cutting speeds and active work at high cutting speeds were more effective in the generation of temperature-induced residual stress.

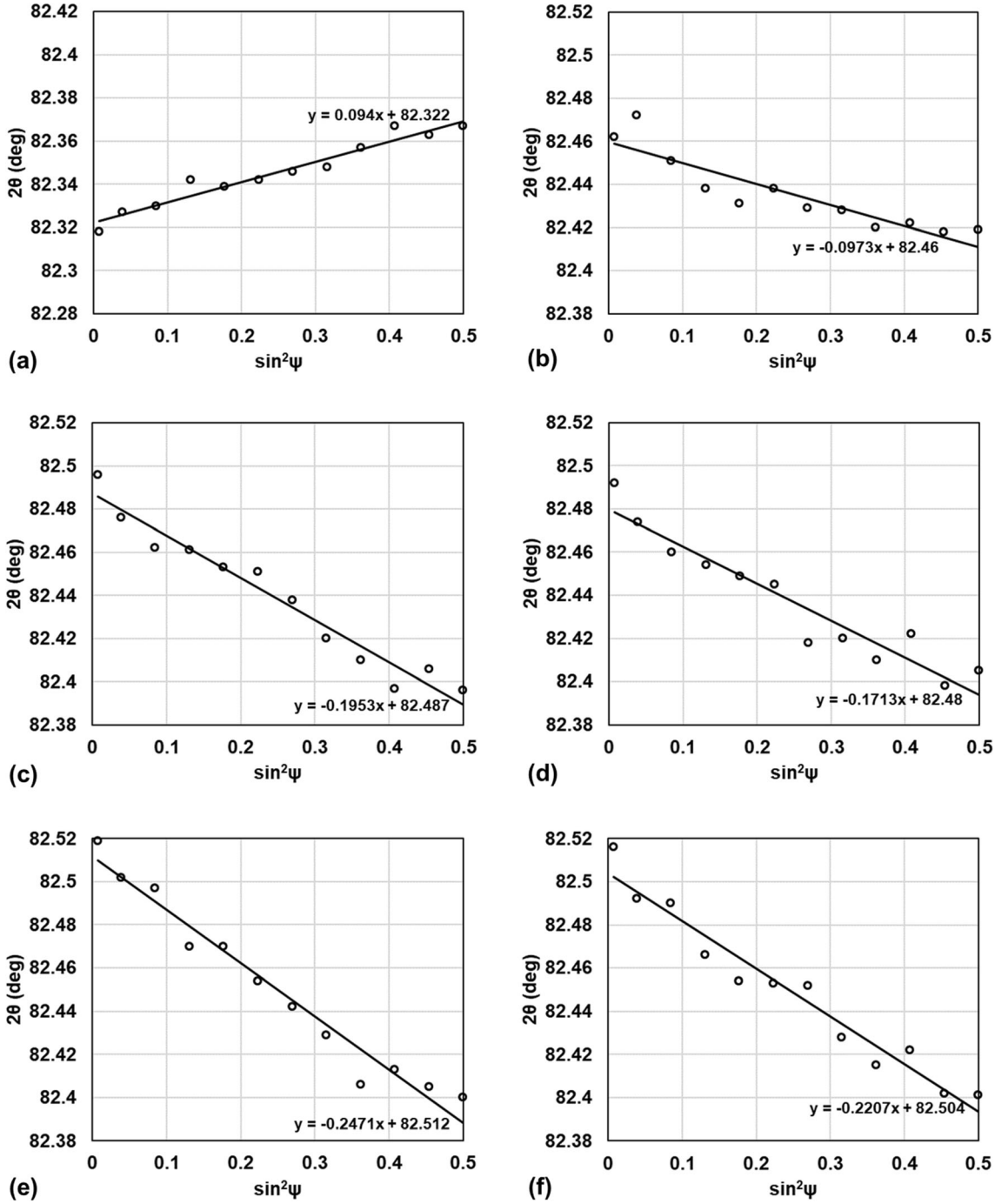

Fig. 7 The 2θ degree vs. $\sin^2\psi$ plot: (a) for the cast specimen; for the machined specimen with parameters (b) V_c = 150 m/min, f_t = 0.15 mm/tooth; (c) V_c = 150 m/min, f_t = 0.3 mm/tooth; (d) V_c = 300 m/min, f_t = 0.15 mm/tooth; (e) V_c = 300 m/min, f_t = 0.3 mm/tooth; and (f) V_c = 450 m/min, f_t = 0.3 mm/tooth

These findings highlight the intricate interplay between cutting parameters, such as cutting speed and feed, and their impact on residual stress generation. The results demonstrate that different combinations of cutting speeds and feeds can lead to varying levels of plastic deformation, temperature changes, and heat accumulation, ultimately influencing the magnitude of residual stresses in the milled workpieces.

4. Conclusions

The study and detection of residual stresses are critical for the selection of cutting parameters to avoid or minimize tensile residual stresses, which are detrimental to the fatigue performance of the machined part, especially for CGI, the material of choice for engine blocks and cylinder heads.

Table 5 Residual stress measurement results obtained from surfaces by x-ray diffraction

Sample #	Milling parameters		Residual stress, MPa	Reliability ± , MPa	Tangential force, N	Power, W	Active work, J
	V_c, m/min	f_t, mm/tooth					
Cast surface	…	…	−107	17	…	…	…
1	150	0.15	+111	12	340.7	852	594.7
2	150	0.3	+224	16	614.6	1536	536.3
3	300	0.15	+196	22	337.0	1685	588.2
4	300	0.3	+283	21	659.9	3300	575.8
5	450	0.3	+257	58	672.5	5043	580.4

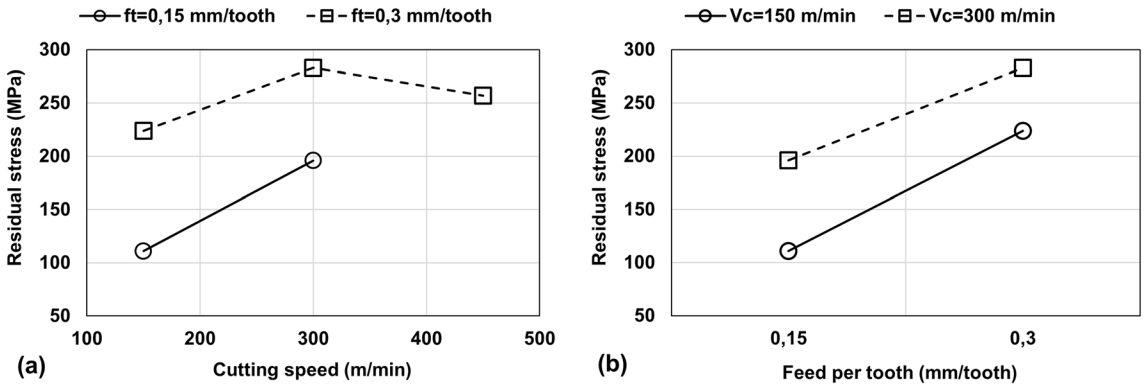

Fig. 8 The effects of (a) cutting speed and (b) feed on the residual stress in the milling operation of GJV-400

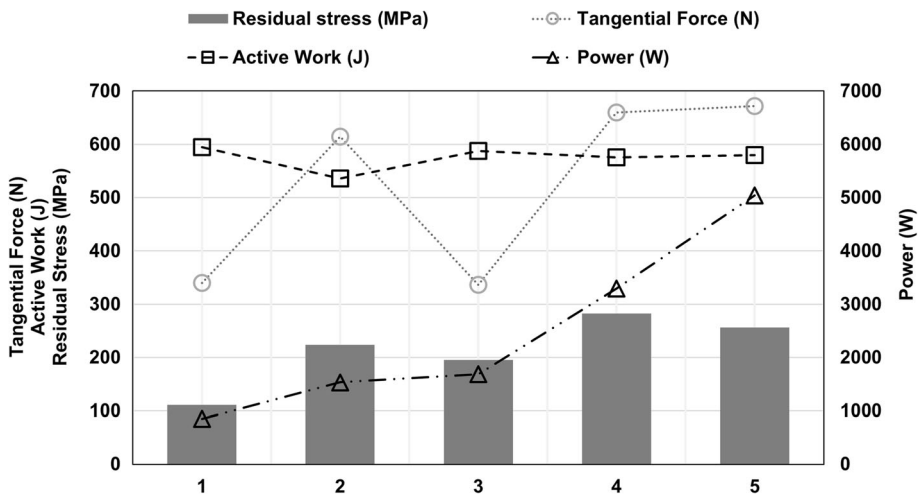

Fig. 9 The effects of tangential force, power, and active work on the residual stress in the milling operation of GJV-400

The analysis of residual stress using x-ray diffraction revealed that the cast specimen exhibited compressive residual stresses on its surface, while the milled workpieces displayed tensile residual stresses. This observation suggests that the milling process induces both mechanical and thermal stresses that contribute to the generation of tensile residual stresses, which are known to have a negative effect on the fatigue strength of the material.

The investigation of different cutting speeds and feeds highlighted the intricate interplay between these parameters and their impact on residual stress generation. Lower feeds were found to contribute to reduced plastic deformation, resulting in relatively lower residual stresses. On the other hand, high feeds induced more plastic deformation, leading to higher residual stresses. The cutting speed also played a role, as higher speeds increased temperatures during milling. However, the reduced machining time limited heat accumulation, resulting in varying levels of residual stresses. The study also showed that the effect of feed on the residual stresses in CGI material is more dominant than the cutting speed.

It is shown that residual stress can be predicted by interpreting tangential force, power, and active work values, which are mechanical energy indicators in milling operations. It is observed that the tangential force representing mechanical

loads has more effect on the residual stresses generated on the workpiece surface after CGI milling than the power and active work representing thermal loads.

These findings emphasize the importance of carefully selecting cutting parameters to control residual stress levels in the milled workpieces. By optimizing cutting speed and feed, manufacturers can manage plastic deformation, temperature changes, and heat accumulation, thereby influencing the magnitude of residual stresses. The knowledge gained from this study can aid in improving the machining processes for CGI, allowing for the production of components with enhanced fatigue strength and performance.

Acknowledgments

We are thankful for the support received from The Scientific and Technological Research Council of Türkiye.

Conflict of interest

The authors declare no competing interests.

References

1. E.C. Reed and J.A. Viens, The Influence of Surface Residual Stress on Fatigue Limit of Titanium, *ASME. J. Eng. Ind.*, 1960, **82**(1), p 76–78. https://doi.org/10.1115/1.3663004
2. F. Mocellin, E. Melleras, W.L. Guesser, and L. Boehs, Study of the Machinability of Compacted Graphite Iron for Drilling Process, *J. Braz. Soc. Mech. Sci. Eng.*, 2004, **26**(1), p 22–27. https://doi.org/10.1590/S1678-58782004000100004
3. M.E. Turan, S. Ozcelik, F. Husem, H. Ahlatci, Y. Sun, and I. Tozlu, The Effect of Head Hardening Process on the Residual Stress of Rails, *Proc. I. Mech. Eng. Part F J. Rail Rapid Transit*, 2018, **232**(2), p 589–595. https://doi.org/10.1177/0954409716679450
4. P.J. Withers, M. Turski, L. Edwards, P.J. Bouchard, and D.J. Buttle, Recent Advances in Residual Stress Measurement, *Int. J. Press. Vessel. Pip.*, 2008, **85**(3), p 118–127. https://doi.org/10.1016/j.ijpvp.2007.10.007
5. S.B. Dronavalli, *Residual Stress Measurements and Analysis by Destructive and Non-Destructive Techniques*, University of Nevada, Reno, 2004
6. K.H. Salman, A.H. Elsheikh, M. Ashham, M.K.A. Ali, M. Rashad, and Z. Haiou, Effect of Cutting Parameters on Surface Residual Stresses in Dry Turning of AISI 1035 Alloy, *J. Braz. Soc. Mech. Sci. Eng.*, 2019, **41**, p 349. https://doi.org/10.1007/s40430-019-1846-0
7. A.H. Elsheikh, S. Shanmugan, T. Muthuramalingam, A.K. Thakur, F.A. Essa, A.M.M. Ibrahim, and O.M. Mosleh, A Comprehensive Review on Residual Stresses in Turning, *Adv. Manuf.*, 2022, **10**, p 287–312. https://doi.org/10.1007/s40436-021-00371-0
8. M. Girinon, F. Dumont, F. Valiorgue, J. Rech, E. Feulvarch, F. Lefebvre, H. Karaouni, and E. Jourden, Influence of Lubrication Modes on Residual Stresses Generation in Drilling of 316L, 15-5PH and Inconel 718 Alloys, *Procedia CIRP*, 2018, **71**, p 41–46. https://doi.org/10.1016/j.procir.2018.05.020
9. A. Rasti, M.H. Sadeghi, and S.S. Farshi, An Analytical Study on Residual Stresses in Drilling of Hardened Steel, *Int. J. Adv. Manuf. Technol.*, 2018, **99**, p 2389–2405. https://doi.org/10.1007/s00170-018-2587-4
10. O. Karabelchtchikova and I.V. Rivero, Variability of Residual Stresses and Superposition Effect in Multipass Grinding of High-Carbon High-Chromium Steel, *J. Mater. Eng. Perform.*, 2005, **14**, p 50–60. https://doi.org/10.1361/10599490522266
11. M. Soori and B. Arezoo, Minimization of Surface Roughness and Residual Stress in Grinding Operations of Inconel 718, *J. Mater. Eng. Perform.*, 2022, **32**, p 8185–8194. https://doi.org/10.1007/s11665-022-07721-4
12. B. Khosrozadeh and M. Shabgard, Effects of Hybrid Electrical Discharge Machining Processes on Surface Integrity and Residual Stresses of Ti-6Al-4V Titanium Alloy, *Int. J. Adv. Manuf. Technol.*, 2017, **93**, p 1999–2011. https://doi.org/10.1007/s00170-017-0601-x
13. L.V. Colwell, M.J. Sinnott, and J.C. Tobin, The Determination of Residual Stresses in Hardened, Ground Steel, *Trans. Am. Soc. Mech. Eng.*, 1955, **77**(7), p 1099–1104. https://doi.org/10.1115/1.4014606
14. Q. Wu, D.P. Li, and Y.D. Zhang, Detecting Milling Deformation in 7075 Aluminum Alloy Aeronautical Monolithic Components Using the Quasi-Symmetric Machining Method, *Metals*, 2016, **6**(4), p 80. https://doi.org/10.3390/met6040080
15. A. Berglund, Criteria for Machinability Evaluation of Compacted Graphite Iron Materials. Ph.D. Thesis, KTH Royal Institute of Technology (2011). Available from http://urn.kb.se/resolve?urn=urn:nbn:se:kth:diva-48430
16. W.H. Bragg and W.L. Bragg, The Reflection of x-rays by Crystals, *Proc. R. Soc. Lond. Ser. A Contain. Pap. Math. Phys. Charact.*, 1913, **88**(605), p 428–438. https://doi.org/10.1098/rspa.1913.0040
17. C.S. Barrett and T.B. Massalski, *Structure of Metals*, Pergamon Press, Oxford, 1981
18. M.E. Fitzpatrick, A.T. Fry, P. Holdway, F.A. Kandil, J. Shackleton, and L. Suominen, *Determination of Residual Stresses by x-ray Diffraction—Issue 2*, NPL, Teddington, 2005
19. I.C. Noyan and J.B. Cohen, *Residual Stress: Measurement by Diffraction and Interpretation, Materials Research and Engineering*, 1987th ed. Springer, New York, NY, 2012
20. H.H. Lester and R.M. Aborn, Behaviour under Stress of Iron Crystal in Steel, *Army Ordnance*, 1925, **6**(6), p 120–127
21. J784A_197108, *Ground Vehicle Standard, Residual Stress Measurement by x-ray Diffraction*, SAE International, Warrendale, 1971
22. ISO 16112:2017, Compacted (vermicular) Graphite Cast Irons—Classification
23. https://www.rigaku.com/products/xrd/smartlab
24. A.L. Mantle and D.K. Aspinwall, Surface Integrity of a High Speed Milled Gamma Titanium Aluminide, *J. Mater. Process. Technol.*, 2001, **118**, p 143–150. https://doi.org/10.1016/S0924-0136(01)00914-1
25. X. Huang, J. Sun, J. Li, X. Han, and Q. Xiong, An Experimental Investigation of Residual Stresses in High-Speed End Milling 7050-T7451 Aluminum Alloy, *Adv. Mech. Eng.*, 2013, **5**, p 1–7. https://doi.org/10.1155/2013/592659
26. D. Hioki, A.E. Diniz, and A. Sinatora, Influence of HSM Cutting Parameters on the Surface Integrity Characteristics of Hardened AISI H13 Steel, *J. Braz. Soc. Mech. Sci.*, 2013, **35**, p 537–553. https://doi.org/10.1007/s40430-013-0050-x
27. B.R. Sridhar, G. Devananda, K. Ramachandra, and R. Bhat, Effect of Machining Parameters and Heat Treatment on the Residual Stress Distribution in Titanium Alloy IMI-834, *J. Mater. Process. Technol.*, 2003, **139**, p 628–634. https://doi.org/10.1016/s0924-0136(03)00612-5
28. M. Salahshoor and Y.B. Guo, Surface Integrity of Biodegradable Orthopedic Magnesium–Calcium Alloy by High-Speed Dry Face Milling, *Prod. Eng.*, 2011, **5**, p 641–650. https://doi.org/10.1007/s11740-011-0341-y
29. I. Ullah, S. Zhang and S. Waqar, Numerical and Experimental Investigation on Thermo-mechanically Induced Residual Stress in High-Speed Milling of Ti-6Al-4V Alloy, *J. Manuf. Process.*, 2022, **76**, p 575–587. https://doi.org/10.1016/j.jmapro.2022.02.039
30. M.L. Silveira, D.A. de Oliveira, A. dos Santos, P.E. de Faria, and A.M. Abrao, Assessment of the Surface Integrity of AISI H13 Tool Steel After Milling with Carbide and Cermet Inserts, *Int. J. Adv. Manuf. Technol.*, 2023, **125**, p 3135–3148. https://doi.org/10.1007/s00170-023-10843-1
31. J.Y. Xu, Q.L. An, and M. Chen, Analysis on Milling Performance of 2024-T351 Aluminum Alloy Using TiAlN Coated Carbide Cutting Tools, *Mater. Sci. Forum*, 2011, **697–698**, p 218–222. https://doi.org/10.4028/www.scientific.net/MSF.697-698.218
32. J. Sun and Y.B. Guo, A Comprehensive Experimental Study on Surface Integrity by End Milling Ti-6Al-4V, *J. Mater. Process. Technol.*, 2009, **209**, p 4036–4042. https://doi.org/10.1016/j.jmatprotec.2008.09.022
33. Q. Wu, D.J. Xie, Y. Si, Y.D. Zhang, L. Li, and Y.X. Zhao, Simulation Analysis and Experimental Study of Milling Surface Residual Stress of Ti-10V-2Fe-3Al, *J. Manuf. Process.*, 2018, **32**, p 530–537. https://doi.org/10.1016/j.jmapro.2018.03.015
34. M.K. Prakash, K.C.S. Chethan, and P.H.P. Thirtha, Residual Stresses Modelling of End Milling Process Using Numerical and Experimental Methods, *Mater. Sci. Forum*, 2020, **978**, p 106–113. https://doi.org/10.4028/www.scientific.net/MSF.978.106

35. M.E. Kara, A.T. Kuzu, and M. Bakkal, The Development of a Hybrid Cutting Model for Workpiece Temperature Distribution via Advection Heat Partition Approach, *Int. J. Adv. Manuf. Technol.*, 2023, **126**, p 4283–4295. https://doi.org/10.1007/s00170-023-11393-2
36. B. Griffiths, *Manufacturing Surface Technology: Surface Integrity & Functional Performance*, CRC Press, Boca Raton, 2001
37. K. Okushima and Y. Kakino, A Study on the Residual Stress Produced by Metal Cutting, *Mem. Fac. Eng. Kyoto Univ.*, 1972, **34**(2), p 234–248

Publisher's Note Springer Nature remains neutral with regard to jurisdictional claims in published maps and institutional affiliations.

Springer Nature or its licensor (e.g. a society or other partner) holds exclusive rights to this article under a publishing agreement with the author(s) or other rightsholder(s); author self-archiving of the accepted manuscript version of this article is solely governed by the terms of such publishing agreement and applicable law.